Author/s:
Malti, A;Brandl, C;Molla, T

Title:
Insights into mechanisms governing the print-bed characteristics in binder jet additive manufacturing

Date:
2025-02-28

Citation:
Malti, A., Brandl, C. & Molla, T. (2025). Insights into mechanisms governing the print-bed characteristics in binder jet additive manufacturing. Powder Technology, 452, https://doi.org/10.1016/j.powtec.2024.120587.

Persistent Link:
https://hdl.handle.net/11343/357272

Powder Technology 452 (2025) 120587

Contents lists available at ScienceDirect

Powder Technology

journal homepage: www.journals.elsevier.com/powder-technology

Insights into mechanisms governing the print-bed characteristics in binder jet additive manufacturing

Abolfazl Malti *, Christian Brandl, Tesfaye Molla

Department of Mechanical Engineering, The University of Melbourne, Victoria 3010, Australia

HIGHLIGHTS

- Microstructural variations across the layers in BJ Printed powder beds investigated utilizing DEM.
- Feedstock PSD impacts local density and particle size along building direction.
- Inter-layer and intra-layer density fluctuations arise from different microstructural mechanisms during printing.
- Optimizing initial PSD as a process parameter enhances powder bed structural homogeneity.

GRAPHICAL ABSTRACT

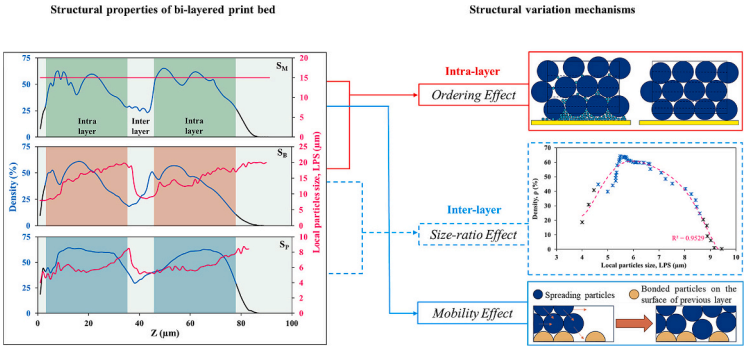

ARTICLE INFO

Keywords:
Binder jet printing
Additive manufacturing
Process – structure – property relationship
Discrete element method

ABSTRACT

While evaluating the overall structural characteristics of print beds in Binder Jet Additive Manufacturing (BJ-AM) is crucial, it fails to capture localized variations that significantly influence the sintering behaviour and final properties of printed samples. This study leverages the Discrete Element Method (DEM) to investigate microstructural heterogeneities in BJ-printed powder beds, with a particular focus on the impact of particle size distribution (PSD) on properties such as green density and local particle size variations along the build direction. The findings reveal that structural non-uniformities in BJ powder beds arise both between and within individual print layers. The inter-layer variations are governed by local 'particle mobility' and 'size ratio' effects, while intra-layer structures are influenced by particle 'ordering' phenomena and packing arrangements. The study provides valuable insights into the intricate relationships between BJ-AM process parameters and powder bed microstructures, facilitating the development of optimized printing protocols to enhance part quality and performance.

1. Introduction

Binder Jet (BJ) printing is one of the Additive Manufacturing (AM) techniques that enables production of complex parts layer by layer. It is particularly valued for its low temperatures shaping process, which helps prevent common high-temperature issues like oxidation and phase transformations in metals. In addition, the possibility of mass production of intricate parts with a diverse range of materials makes BJ printing a

* Corresponding author.
E-mail addresses: amalti@student.unimelb.edu.au, a.malti@unimelb.edu.au (A. Malti).

https://doi.org/10.1016/j.powtec.2024.120587
Received 11 November 2024; Received in revised form 19 December 2024; Accepted 23 December 2024
Available online 25 December 2024

promising technology for applications ranging from rapid prototyping to customized medical implants [1–5]. BJ printing involves a powder spreading process followed by selective injection of a liquid binder, which bonds the powder particles together. This process is critical as it sets the structure for post-processing steps, such as infiltration and sintering, which are employed to enhance the part's density and mechanical properties [6,7].

The sintering behaviour of BJ printed parts is affected by the arrangement of particles and the particle-pore structure after the layer-by-layer printing process [8]. A typical example is the anisotropic shrinkage often observed during sintering of BJ printed parts because of the heterogenous structure along the build direction. Controlling the structural variations in BJ printed samples requires understanding the influence of printing parameters such as layer thickness, particle size distributions (PSD) together with the mechanisms governing particle rearrangements including segregation during the layer-by-layer printing [9–12]. This is vital for not only controlling processing defects like shape distortions after sintering but also helps to enhance performance properties of the final product.

The structures of BJ printed samples are often characterized by parameters like the "average green density" and "average particle size". While these metrics are suitable for scenarios where particles are evenly distributed, the BJ printing process inherently introduces variations in density and particle size distribution along the build direction causing anisotropic shrinkage and possibly shape distortion during sintering [13,14]. Therefore, it is crucial to characterize the structural heterogeneity of BJ printed samples to control processing defects during sintering. It is also critical to understand the mechanisms governing the print-bed formations during spreading of powders in BJ printing. In this regard, Rios et al. [15] utilized high-resolution synchrotron X-Ray computed tomography (SXCT) to study the density fluctuations in BJ printed samples. They presented possible microstructural mechanisms for variations in density of BJ printed samples across the build direction including formation of voids in between layers caused by spreader-particles and binder-particles interactions. However, their analysis did not thoroughly explore the variations in packing density as well as particle size across the build direction of the print-bed in a way to correlate with the printing parameters.

By employing computational approaches based on Discrete Element Method (DEM), it is possible to simulate, measure and analyse the characteristics of BJ printed samples [16–18]. These techniques can be used to unravel the detailed mechanisms of powder bed formation during BJ printing and thereby enable optimization of printing parameters to reduce structural heterogeneities causing anisotropic shrinkage during sintering. However, to the best of our knowledge, no computational studies have explored the mechanisms governing the microstructural variations along the build direction, particularly by considering both inter-layer and intra-layer regions of BJ printed powder beds.

This paper aims to shed light on the mechanisms controlling powder bed formation in BJ printing, with a focus on density variations and particle size distribution along the build direction. Capitalizing on our previous work [19], which addresses the multi-layer powder deposition during BJ printing and its impact on sample structure, the current study explores both the inter-layer as well as intra-layer characterises of BJ printed samples using various powder feedstocks. The study uses computational approaches based on DEM for simulation of powder bed formation during BJ printing of stainless-steel powders. By systematically choosing the initial PSD, it is possible to control the mechanisms of powder bed formations and hence achieve structural homogeneity, including packing density and pore/particles arrangements in BJ printed samples. The findings of this study will deepen the understanding of BJ printing process - structure relationships and help in developing optimized printing protocols for wide range of applications.

2. Methodology

2.1. Governing equations

The DEM model applies Newton's second law to determine the translational and rotational motion equations for particle *i*, which are defined as follows:

$$m_i\frac{dv_i}{dt} = \sum_j \left(F_{ij}^t + F_{ij}^n\right) + F_g \tag{1}$$

$$I_i\frac{d\omega_i}{dt} = \sum_j \left(T_{ij}^t + T_{ij}^r\right) \tag{2}$$

where m_i, v_i, υ_i and I_i are the mass, translational velocity, rotational velocity, and moment of inertia of particle *i*, respectively. As shown in eq. 1, the tangential force F_{ij}^t, normal force, F_{ij}^n and gravitational force F_g are the forces exerted on particle *i*. T_{ij}^t and T_{ij}^r are the torque produced by the tangential force from particle *i* and the torque from rolling friction that inhibits the rotation of particle *i,* respectively:

$$T_{ij}^t = R_i{*}F_{ij}^t \tag{3}$$

$$T_{ij}^r = -\mu_r{*}R_i{*}F_{ij}^n{*}\widehat{\omega_i} \tag{4}$$

where, R_i, μ_r and $\widehat{\omega_i}$ denote the radius of particle *i*, rolling friction coefficient and unit angular velocity ($\widehat{\omega_i} = \frac{\omega_i}{|\omega|}$).

The current study utilized the Hertz-Mindlin contact model [20–22] which include both normal and tangential contact forces among particles and between particles and boundary surfaces (e. g., substrate and roller). The tangential force F_{ij}^t is calculated by accounting for the relevant contact dynamics and damping effects as:

$$\begin{cases} \boldsymbol{F_{ij}^t = F_{c,ij}^t + F_{d,ij}^t}, \\ F_{c,ij}^t = -min\left\{F_f \middle| 8G^*.\epsilon^t\sqrt{R^*.\epsilon^n}\right| \right\} \\ F_{d,ij}^t = \sqrt{\frac{80}{3}}\beta\left[G^*.m^*.\sqrt{R^*.\epsilon^*}\right]^{1/2}u_{ij}^t \end{cases} \tag{5}$$

where, F_f, ϵ^n, ϵ^t, β and u_{ij}^t are the friction force, normal and tangential overlap, normal damping coefficient, and tangential relative velocities between particles *i* and *j*. G^*, m^*, R^* and ϵ^* are the equivalent shear modulus, equivalent mass, equivalent radius, and equivalent interparticle overlap, respectively. To consider the inter-particles cohesiveness, the surface energy-dependent cohesive forces is added to Hertz-Mindlin contact model to integrate the Van der Waals forces into the normal contact forces between particles in the following way [23,24]:

$$\begin{cases} \boldsymbol{F_{ij}^n = F_{c,ij}^n + F_{d,ij}^n}, \\ F_{c,ij}^n = \frac{4E^*}{3R^*}r^3 - 4\sqrt{\pi.r^3.\gamma.E^*} \\ F_{d,ij}^n = -\sqrt{\frac{20}{3}}\beta\left[E^*.m^*.\sqrt{R^*.\epsilon^*}\right]^{1/2}u_{ij}^n \end{cases} \tag{6}$$

where, u_{ij}^n is the normal relative velocities due to collision between particles *i* and *j*, and E^* is the equivalent Young's modulus. The

parameter γ is the excess surface energy which can be calculated by considering the difference between free surface energy and interface energy [19]. Having the Poisson's ratio of particles *i* and *j* (υ_i and υ_j), the equivalent parameters can be calculated as:

$$\begin{cases} E^* = (E_i{}^*E_j)\Big/\Big[E_i\left(1-\upsilon_j^2\right) + E_j\left(1-\upsilon_i^2\right)\Big], \\ G^* = (G_i{}^*G_j)\Big/\big[G_i(1-\upsilon_j) + G_j(1-\upsilon_i)\big], \\ m^* = (m_i{}^*m_j)\big/(m_i+m_j), \\ R^* = (R_i{}^*R_j)\big/(R_i+R_j). \end{cases} \tag{7}$$

Note that the variable *r* in *eq.* (6) is the contact radius obtained from the normal overlap ϵ^n through the equation:

$$\epsilon^n = \frac{r^2}{R^*} - \sqrt{\frac{2\pi\gamma r}{E^*}} \tag{8}$$

Schematics demonstrating all the normal and tangential forces between two particles is shown in Fig. 1(a). Fig. 1(b) depicts the constitutive model that governs the interaction between two particles when particles undergo deformation as shown by the normal and tangential displacements, δ^n and δ^t, respectively [22]. The normal and shear deformations can be modelled by a linear spring *(k)* and a viscous dashpot *(η)*. Moreover, when one of the particles has an infinite diameter, it can be envisioned as a wall, enabling us to simulate collisions between a particle and a wall.

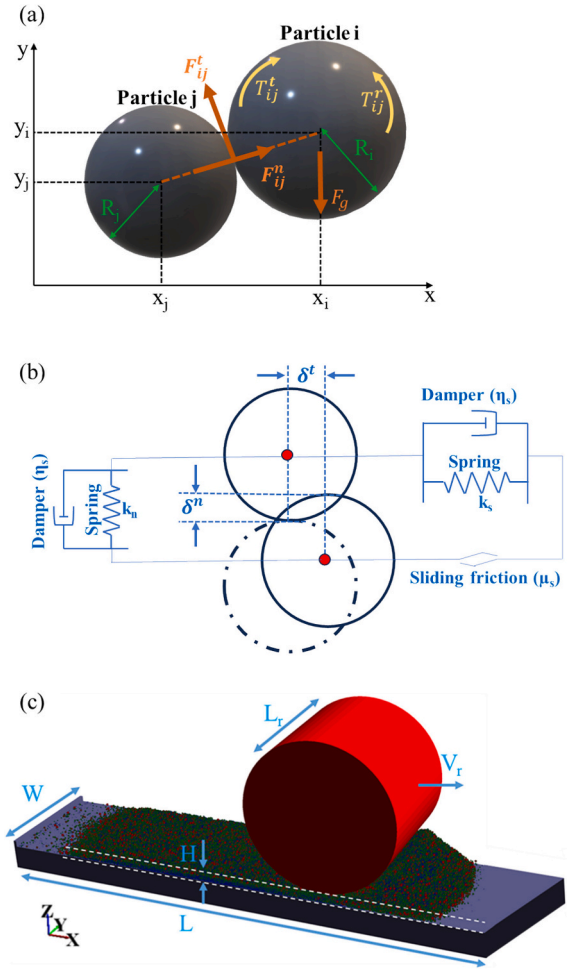

Fig. 1. Schematics of a) interaction forces between powder particles in DEM model; b) constitutive behaviour describing collisions between particles; c) powder-spreading process.

An open-source DEM software called MUSEN is utilized to simulate the powder spreading process in current study [25]. In DEM simulation, it is crucial that the time step Δt used to compute incremental contact forces and particle displacements is smaller than a characteristic time Δt_c, referred to as the Rayleigh time step [26]. In this study, the simulation time step Δt is determined according to MUSEN's guidelines, which consider the simulation scale and material properties:

$$\begin{cases} \Delta t < \Delta t_c, \\ \Delta t_c = min\left[\dfrac{\pi R}{0.163p + 0.877}\sqrt{\dfrac{\rho}{E}}\right] \end{cases} \tag{9}$$

2.2. Simulation conditions and DEM parameters

The materials as well as process parameters used for DEM simulation of the powder spreading process in the current work are summarized in Table 1. Data for the Poisson ratio, coefficients of restitution, sliding and rolling friction for 316 L stainless steel granules were obtained from literatures [17,27–29]. The excess surface energy density, γ is a critical parameter influencing the dynamic behaviours of powder particles and requires careful calibration of the model with experimental results. In our previous research, calibration of the excess surface energy was performed by simulating experimental techniques, lifting hollow cylinder and fixed funnel methods, commonly employed to measure the flowability of powders [19]. A similar approach has been used for the powders in the current study and the excess surface energy is found to be 0.1 mJ/m^2. This value is consistent with the findings of other researchers who studied powders of the same material [16,28,30]. For more details on the calibration procedures, readers can refer to [19]. In addition, it is important to note that in DEM simulations, reduced magnitudes of Young's modulus are used compared to actual values. This approach helps to extend the Rayleigh critical time-step limit, enabling more manageable computational simulations without significantly impacting the results, a practice commonly adopted in similar studies [16,27,30]. Moreover, to simplicity the problem, the variations in friction conditions between powder-powder and powder-wall (substrate and roller) interactions are ignored, as the materials for powder, substrate, and roller are all assumed to be made of 316 L stainless steel.

Regarding the process parameters, the layer thickness (H) and roller velocity (V_r) are set at 50 μm and 25 mm/s, respectively. This is typical for experiments in this field, especially for particle size distributions similar to those used in our study [7,31]. The roller velocity was determined from the process map developed in our previous research, designed to ensure that the dynamics and flow of the particles remain

Table 1
Summary of model, materials and process parameters.

Parameters	Value	References
Young's modulus, *E* [*Pa*]	2.2 × 10^9	[16,30]
Theoretical density, ρ_t [kg/m^3]	7800	[29]
Poisson's ratio, υ [−]	0.3	[29]
Coefficient of restitution, *e* [−]	0.64	[27–29]
Coefficient of sliding friction, μ_s [−]	0.6	[17,29]
Coefficient of rolling friction, μ_r [−]	0.085	[17,29]
Surface excess energy, γ [mJ/m^2]	0.1	
Layer thickness, *H* [μm]	50	
Roller velocity, V_r [*mm/s*]	25	

unaffected by the roller's movements, positioning them within the insensitive region of the process parameters. The study employs simulation of multi-layer powder deposition for three different types of samples involving distinct powder size distributions (PSDs). These are:

i) Mono-sized powders with a diameter $D = 15$ μm,
ii) Bimodal powders with 90 *vol%* of coarse particles of diameter, $D_c = 20$ μm and 10 *vol%* of fine particles with diameter, $D_f = 8$ μm; and
iii) Size distributed powders with $D_{10} = 4$ μm, $D_{50} = 15$ μm, and $D_{90} = 20$ μm.

Henceforth, samples corresponding to the three PSDs above will be referred to as 'S_M', 'S_B' and 'S_P' respectively.

Note that feedstock powders in additive manufacturing processes typically consist of particles with continuous size distributions. Even in so-called mono-sized and bimodal cases, a certain degree of size variation is inevitable. However, the use of mono-sized and bimodal powders in this study is meant to simplify the system and isolate the fundamental mechanisms controlling powder bed formation in BJ printing under idealized conditions. Furthermore, these scenarios represent extreme cases of PSDs. All other PSDs, which fall between these two extremes, are likely to experience mechanisms that are a combination and/or subgroup of the extreme scenarios.

2.3. Simulation of multi-layer powder spreading

Powder spreading using a roller is a common technique in both industrial additive manufacturing machines and research studies [19,23,32]. The model shown in Fig. 1(c) is designed based on methods from our previous study [19] and mimics a typical setup with a non-rotating roller and a rectangular substrate [33]. The dimensions of the substrate are given by L*W, where L is the length and W is the width of the spreading area. To reduce computational costs, the substrate's width is significantly less than what is used in practical experiments. Instead, periodic boundary conditions are applied along the y-direction to reduce the wall effects during the spreading process. The radius of the roller is denoted by R_r, and its length, L_r is equal to the width of the substrate in the y-direction.

In binder jet printing, binder droplets between particles in the previously deposited layers prevent fine particles of the spreading layer from sinking down, i.e., percolation. However, it is difficult to incorporate effect of the liquid binder in DEM techniques without coupling with computational fluid dynamics (CFD) solvers. For example, Penny et al. [34] simulated the multi-layer spreading of particles without limiting percolation of particles and as a result fine particles from a new layer have been shown to mix with the previously deposited layer, affecting the density and particle size distribution within layers. In another study, Li et al. [35] explored the density of different powder layers deposited on both loose/mobile and fixed/immobile previously printed layers. However, they did not account for the role of the binder, which could potentially lead to fine particles percolating into the previous layer and deviations from the actual situation.

In this study, the spreading of a new powder layer is modelled by considering the approximate surface geometry of the previously deposited layer (print bed). This is achieved by carefully identifying the different types of particles within the print bed. Fig. 2(a) provides a schematic representation of a powder bed, where the yellow box illustrates the liquid binder surrounding the particles. Based on their interaction with the binder, the particles in the print bed can be classified into three categories: (i) fully immersed particles located in regions with sufficient binder; (ii) partially immersed particles; and (iii) non-immersed (unbonded) particles in areas with insufficient binder.

The surface geometry of the print bed is constructed by considering the upper boundary of the binder along with non-immersed (unbonded) particles and partially immersed particles that protrude more than 50 % above the binder region. Fig. 2(b) illustrates the resulting surface, where the roughness caused by non-immersed and partially immersed particles is depicted in grey. This approach is employed to prevent the percolation of fine particles during the simulation of the new layer spreading process. The methodology is applied in a way to prevent particle splash and destruction of the powder bed due to particle-wall overlaps. Note that the properties of the first layer are measured after spreading and are unaffected by the formation of subsequent layers. On the other hand, the properties at the interlayer and in the newly deposited layer are assessed after the deposition of the second layer. The approach allows for the incorporation of the liquid binder's effects during the simulation of multi-layer powder deposition (spreading) in BJ printing, without incurring higher computational costs associated with coupling DEM and CFD solvers.

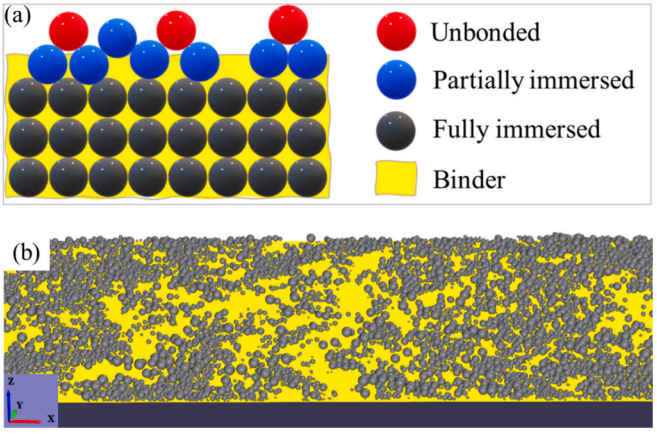

Fig. 2. Schematics of a) powder bed including different particles and binder in between; b) method to mimic the role of binder in a bi-layer powder bed.

3. Results and discussions

3.1. Microstructure characterization of multi-layered powder bed

In this section, the variations of powder-bed density and local particle size (*LPS*) across the build direction for the three samples (i.e., S_M, S_B and S_P) are analysed. To understand the effect of layering, the analysis is performed over two regions of the print-bed. These are: i) between print-layers or inter-layer region and ii) within the print layer or intra-layer region. Fig. 3(a) shows the density and *LPS* across the height of bi-layered powder bed measured using 100 sub-domains across the build direction (z-axis) for the three samples. The intra-layer regions (also known as body of each layer) are distinguished from the inter-layer regions by coloured backgrounds. In addition, the black colours on the plots represent regions near the substrate and free surface of the powder bed, which are not considered part of either the intra-layer or inter-layer of the powder bed.

Structure of the print-bed across the different regions are characterized by coefficients of variations of density (ρ_{cv}) and *LPS* (LPS_{cv}). The coefficients of variation are defined in Eqs. (12) and (13), where ρ_{st} and LPS_{st} represent the standard deviation of local density and *LPS,* and $\bar{\rho}$ and $\overline{LPS}$ are the corresponding average values, all measured along the z-direction using a moving domain.

$$\rho_{cv} = \frac{\rho_{st}}{\bar{\rho}} \tag{12}$$

$$LPS_{cv} = \frac{LPS_{st}}{\overline{LPS}} \tag{13}$$

It is worth noting that a higher value of ρ_{cv} and LPS_{cv} indicates a greater degree of structural heterogeneity and more pronounced fluctuations of the corresponding properties. Figs. 3(b) and (c) depict the

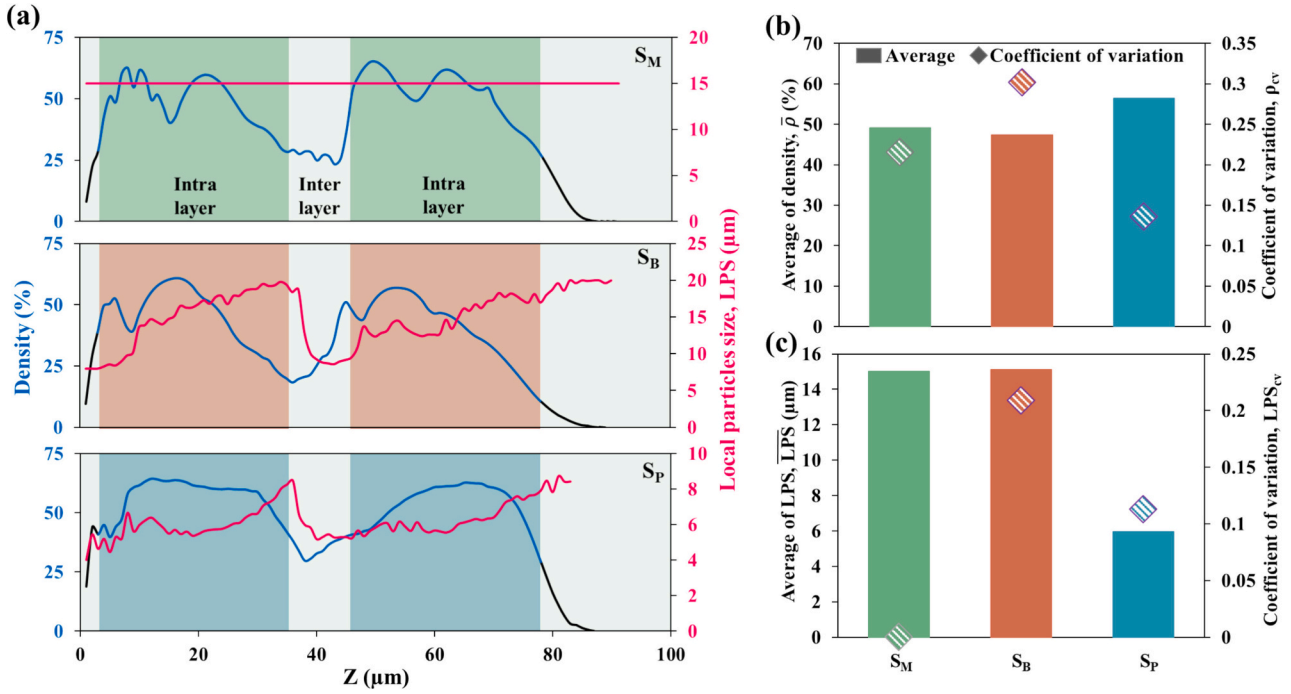

Fig. 3. a) Plots of density and local particle size, *LPS*, as a function of height for samples with different initial particle size distribution. The intra-layer regions are highlighted by coloured backgrounds and the regions near the substrate and free surface of the powder bed are plotted by black colour; b) average and coefficient of variation of intra-layer density and c) average and coefficient of variation of intra-layer *LPS*.

average and variation coefficients of density and *LPS* in the intra-layer regions of the three samples, respectively. The mechanisms behind microstructural formations in each sample are thoroughly explored in the next sections.

3.2. Inter-layer characteristics of print bed

As illustrated in Fig. 3(a), a pattern of density variations is evident, characterized by fluctuations between maximum within the layers and minimum between the layers (i.e., fluctuations periodic with the layer thickness). It is also evident that both the inter-layer as well as intra-layer fluctuations can affect the overall density of BJ printed samples. Previous studies [15,36] have shown the fluctuating nature of density and particle size in BJ printed samples. A few mechanisms have also been proposed to explain the heterogenous nature of microstructures between successive layers. Rios et al. [15] explained the mechanism of formation of inter-layer density variation during BJ printing based on spreader-particle and binder-particle interactions. This is commonly referred to as cratering effect causing large voids (porosities) between successive layers. Additionally, Evan et al. [36] reported particle segregation along the build direction in BJ printed samples, attributing it as another factor to density variations both within and between layers. The results of the current study align with previous research efforts. However, the behaviour of density and *LPS* in the inter-layer regions of the three samples, each with different initial particle size distributions, show notable variations, see Fig. 3(a). This observation indicates the

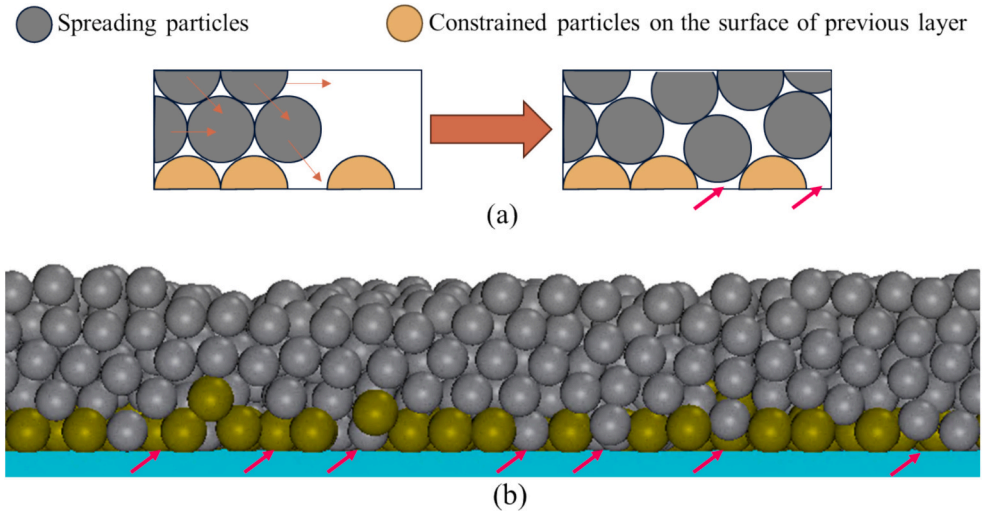

Fig. 4. a) Schematics showing the role of constrained particles from previous layer in the formation voids; b) Simulated results of mono-sized powder bed corresponding to (a). Red arrows show the inter-layer voids. (For interpretation of the references to colour in this figure legend, the reader is referred to the web version of this article.)

possibility of multiple mechanisms involved in the formation of the inter-layer region. The following section will investigate these mechanisms in greater detail.

3.2.1. Mechanisms governing the inter-layer characteristics of the print-bed

In the case of sample with mono-size distribution of powders, the large voids between particles affect the inter-layer density. The formation of these large inter-layer voids is mainly attributed to the constrained mobility of particles from the previous layer (particle mobility effect) as shown schematically in Fig. 4. During spreading of a new layer, the movement of particles in the previous layer is constrained by the binder, affecting the powder flow within the inter-layer region [37]. This limited mobility prevents the ability of new particles to fill the surface voids of previous layer causing large voids in the inter-layer regions. Fig. 4(b) shows simulated interface of a bi-layer powder bed containing mono-sized particles, where yellow particles belong to the previously deposited layer, which are constrained by binder and grey ones are particles from the new layer. Although some of the large voids created by the interactions between the spreader and particles in the inter-layer region are partially filled by new particles, most of these surface voids persist, and new pores are even likely to form between layers. This is consistent with Rios et al. [15] observations that the formation of large voids at the surface of layer is due to the spreader-particles interactions and partial filling of these voids are the main reasons for lower density between layers. In our previous study [19], it was also observed that the force applied by roller to the spreading particles largely influences the flow, dynamics and positioning of these particles, particularly those placed in the vicinity of the roller.

It is worth highlighting that the "particle mobility effect" explained for mono-sized powders may not govern density fluctuations in BJ printed samples with a different PSD. Particles segregation with varying degrees of severity can occur during the formation of print-beds with bi-modal (e.g., S_B) and/or size distributed (e.g., S_P) particles. This segregation is primarily due to percolation of fine particles, which tend to concentrate at the bottom of the spread layer. Percolation of fine particles can fill the voids created at the surface of the previously deposited layer, thereby increasing the density of the inter-layer region. Experimental findings demonstrate that utilizing a wider particle size distribution enables fine particles to percolate to the inter-layer regions between subsequent powder layers and occupy gaps between print layers [37,38]. This is also advantageous during sintering as it promotes the reduction of pores. Figs. 5(a) and 5(b) schematically depict comparison of the distributions of pores while spreading mono- and bi-modal sized powders, respectively. The yellow particles are the surface particles of the previous layer that are immobile during spreading of a new layer. In addition, Figs. 5(c) and 5(d) shows simulation results corresponding to mono- and bi-modal sized powders, respectively, displaying the interlayer region from the top. The height of interlayer region is considered equal to the diameter of largest particles. In the case of bi-modal powders, most of the remaining pores in the inter-layer region are filled by fine particles that have percolated down. This also explains the lower *LPS* observed in the inter-layer region for S_B and S_P samples. Therefore, formation of voids between successive layers due to low particles mobility cannot necessarily be the only mechanism causing density drop in the inter-layer region.

The drop in density in the inter-layer region for samples S_B and S_P might be to do with segregation of particles between layers followed by uneven distributions of coarse and fine particles. It is well-known that segregation of particles causes varying densities, as areas with various fractions of fine and coarse particles will have different packing density [39]. Areas with predominantly fine and/or coarse particles are likely to achieve lower green densities and, obviously, an optimum *LPS* would lead to the maximum density [40].

One factor contributing to particle segregation is the dynamics of the spreading process. Movement of the roller during spreading causes significant agitation of the powder compact below the roller. Despite the brief spreading time, the short segregation distance allows powders to move down during the spreading process. However, since a pile of powder particles relaxes before the movement of the roller, further investigation is needed to determine whether the segregation is caused by the relaxation or spreading process.

Fig. 6 shows the *LPS* along z axis after relaxation of a powder pile in front of the roller for feedstocks corresponding to S_B and S_P. The results demonstrate that no considerable particles segregation happened during the relaxation step and hence all the segregation observed in the powder bed is caused by the shear force applied by roller during the spreading process. Henceforth, the term "shear-induced segregation" will be used to show the particle segregation caused by roller movement.

Fig. 7(a) shows simulation results depicting the variations of density and *LPS* along the build direction of S_P print-bed. The results align well with the experimental measurements (i.e., by using SEM and XCT) [41]. Sergi et al. [41] demonstrated the presence of inter-layer porosities between dense layers of a BJ printed sample produced from powders with a D_{50} of 13 μm, which closely matches with the D_{50} particle size used in this study.

In Fig. 7, Roman numbers are used to indicate the distinct and repeating regions across the thickness of successive layers. The inter-layer regions (i.e., regions *i* and *iii*) can be characterized by non-optimal local particle size distributions and coarse to fine particle size ratios, resulting in high rate of changes in local density and *LPS*. In fact,

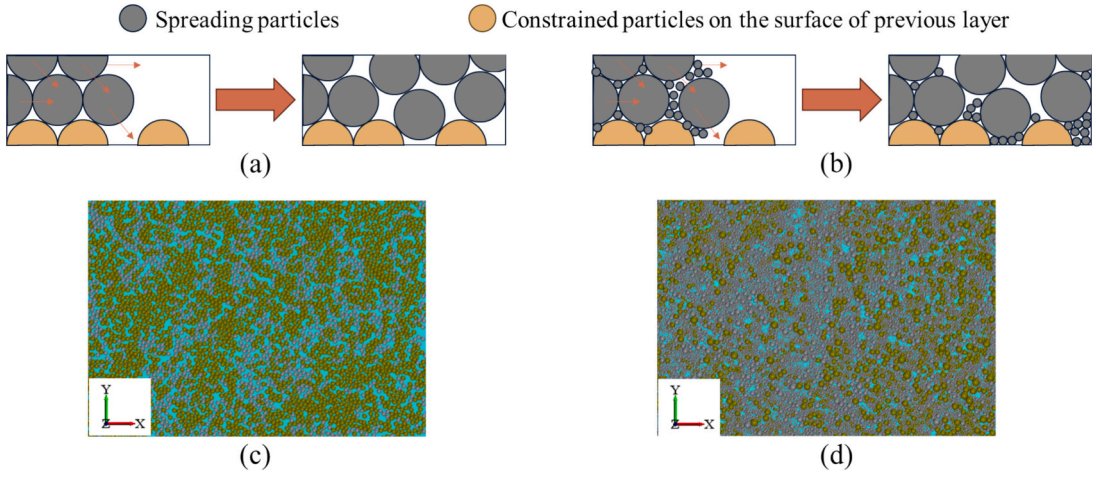

Fig. 5. a and b) Schematics of inter-layer region formation in monomodal and bimodal powder bed; c and d) The interlayer region after spreading the second layer with mono-sized and bi-modal powders, respectively.

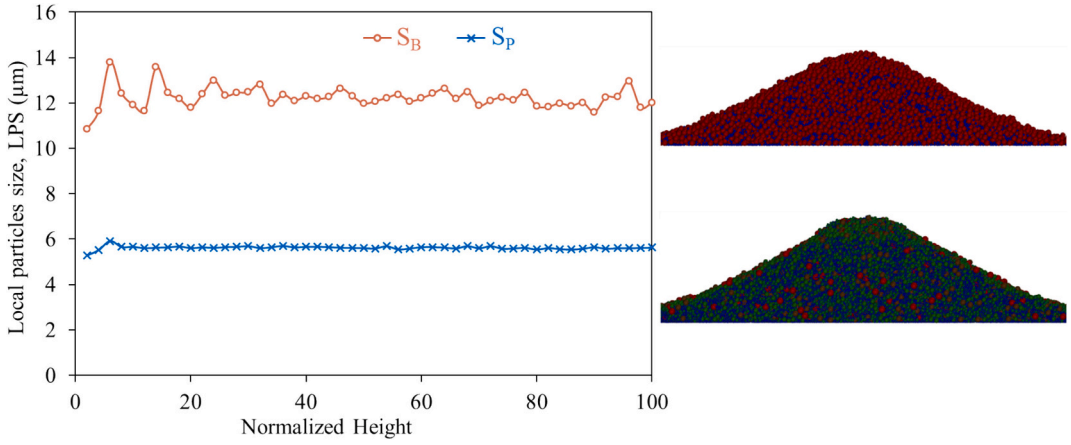

Fig. 6. The change of *LPS* along the z axis within the collapsed and relaxed powder pile in S_B and S_P.

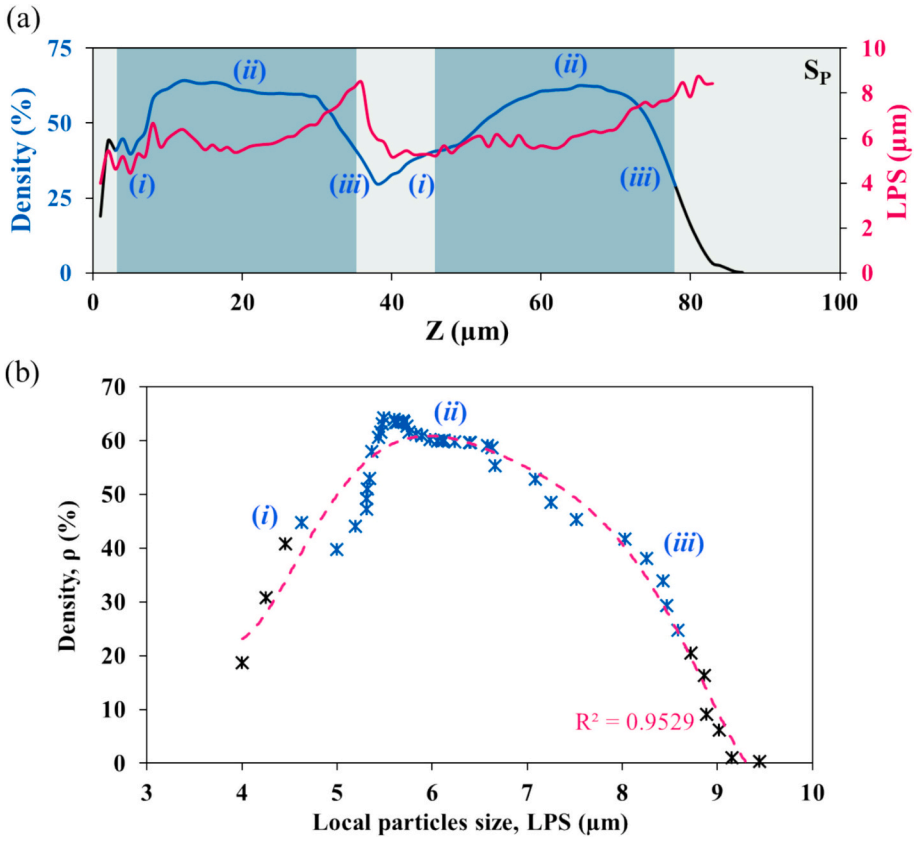

Fig. 7. a) Density and *LPS* across thickness of a bi-layered print bed with S_P powders. The dashed line shows the *LPS* of the powder pile; b) The correlation between density and *LPS* in print beds with S_P powders.

the drop in the local inter-layer density starts from a critical region inside the layers as a result of non-optimal ratio of course to fine particle sizes and the associated phenomena (i.e., size ratio effect). A similar behaviour is also observed in powder bed containing bi-modal powders. By comparing the S_P and S_B samples in Fig. 3(a), one can discern that a smaller deviation from the ideal coarse-to-fine particle size ratio (i.e., a less pronounced size ratio effect) results in a lower rate of density reduction in S_P compared to S_B. Fig. 7(b) illustrates the correlation between density and *LPS* in the first layer of S_P, where deviation from optimal *LPS* (i.e., state *ii*) causes drop in local density. This is also found to be consistent with previously reported studies [1,42–44].

Fig. 8(a) shows the theoretical relationship between density and fraction of coarse particles with schematic representations for the microstructural states (*i* to *iii*) at different points [44,45]. Comparison of the theoretical microstructural states with the DEM results shown in Fig. 7(a) reveals that in the inter-layer region of bi-layer print bed, two low density states, i.e., states *i* and *iii*, are in close proximity, leading to drop in density compared to the intra-layer region (state *ii*). The DEM results from the current study are not only in-line with theoretical analysis [43] but they are also consistent with experimental observations. For instance, in a study to investigate the role of printing parameters on the packing density of BJ printed samples, Chen et al. [45] showed that powder bed with wide PSD (Fig. 8(c)) exhibits higher density than powder bed containing solely large (Fig. 8(d)) or fine (Fig. 8

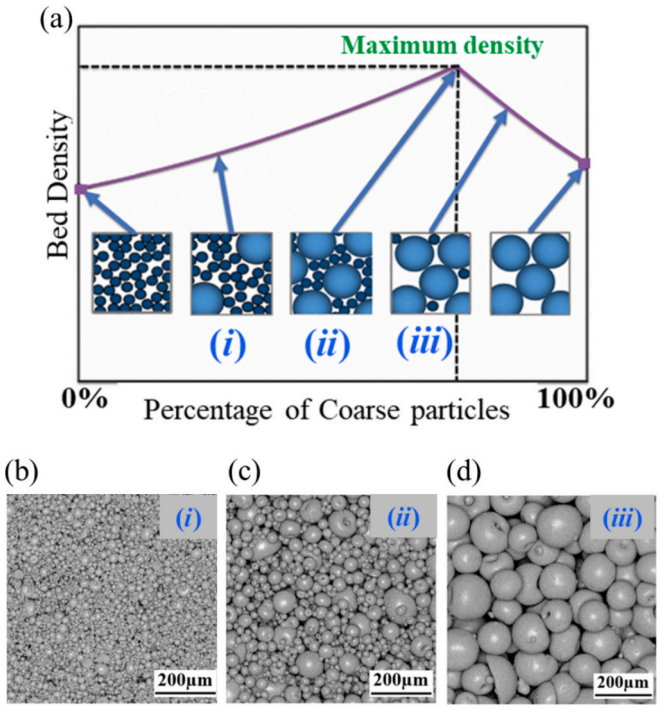

Fig. 8. a) Theoretical relationship between density and fraction of course particles with schematics of microstructures. Corresponding to the states shown in Fig. 7(b), reused from [44]. b – d) Optical laser images of different powder beds containing various PSDs [45], reproduced with the permission of Elsevier.

(b)) particles.

3.3. Intra-layer characteristics of print bed

As shown by Fig. 3(a), the density as well as *LPS* fluctuate with the height of the powder bed in all samples. This structural variation is not solely due to inter-layer characteristics, but intra-layer phenomena can also lead to structural fluctuations across the height of the BJ printed samples. Furthermore, the fluctuations in density as well as *LPS* varies with particle size distribution. The intra-layer density for S_P samples is observed to be higher than both S_M and S_B samples. Additionally, a comparison of the coefficient of variation of density (ρ_{cv}) reveals that S_P samples show the least local density fluctuations within the layers, while S_B sample exhibited the highest density fluctuations. Sample with a distribution of powders from 4 to 20 µm leads to formation of high-density powder bed with a homogeneous intra-layer structure which encompasses majority of the print-layer thickness. These observations imply that deposition of powders with a wider distribution of particle size is useful to enhance packing density as well as homogeneity of the microstructure.

3.3.1. Mechanisms governing the intra-layer characteristics of the print-bed

It has been widely reported that there is a tight correlation between the packing density of particulate matter and their PSD. Therefore, one may expect a relationship between the PSD and density of powder bed. However, Fig. 3(a) shows that packing density could also fluctuate within layers for samples with mono-size distribution of powders indicating the presence of other mechanisms affecting density and its homogeneity.

Fig. 9(a) to (c) show schematics of the powder beds for the three types of samples together with the corresponding density variations across the first layer including snapshots of the powder bed from the DEM simulation. The black colours on the plots of height vs density shows the regions which are not considered as the intra-layer of the powder layer. As shown in Fig. 9(a), the primary cause of intra-layer density fluctuation in S_M samples is the formation of sub-layers with high concentration of voids between particles at specific heights along the z-direction (due to the arrangement of mono-sized particles). This leads to "ordering effect" causing density fluctuation within the layers. Similarly, in the case of bimodal powders sample (see Fig. 9(b)), the severe particles segregation cause regions with different concentration of voids across the z direction. The sub-layers causing ordering effect are distinguished by dashed lines in S_M and S_B.

Existence of ordering effect in other materials like liquids, colloids and particulate systems leading to similar fluctuations in density have been reported by several researchers. For instance, it is shown in [46,47] that the void fraction in powder bed containing mono-modal particles is smallest at the heights corresponding to the centres of the particles. Kim [48] also reported that at microscopic length scales, where the continuum model for dense fluids like liquids or colloidal dispersions is not applicable, the density fluctuations of the fluid confined between two solid walls are influenced by the position of the central particles and the ordering of dense fluids.

The rate of change in particle size inside the layers of S_B samples is higher than in S_P, i.e., larger LPS_{cv} in S_B shows less particle size homogeneity. The correlation between density and *LPS* in S_B and S_P indicates that there is an optimal *PSD* within the layers that results in the highest intra-layer density. Although smaller local particle size increase is observed in S_P, see Fig. 3(a), the gradual size variation along the z direction within the layers (inside the blue border in Fig. 9(c)) prevents distinct layering and notable density fluctuation that occur in bimodal case. In other word, the intra-layer particle size segregation in S_P is not as pronounced as in S_B. However, in the top region of the deposited bed (i.e., for S_P), lack of the particle size distribution resulted in more voids, which was discussed in Sections 3.2 focusing on the inter-layer features.

As shown by the density coefficient of variation, ρ_{cv}, in Fig. 3(b), the intra-layer density fluctuation in S_M is less than that in S_B, while the intra-layer average densities in these two samples are almost the same. This difference in ρ_{cv} might be due to the more regular distribution of pores in mono-sized samples compared with bi-modal one. In other words, the presence of under-populated voids between particles causes smaller density fluctuation within the layers in S_M. In contrast, a powder bed containing bimodal powder with non-optimal coarse-to-fine size and volume fractions may result in various spatial arrangements of particles, leading to a heterogeneous powder bed with both under-populated and over-populated voids. This can also be demonstrated by comparing the density variations across the height as shown in Fig. 9a and b.

The difference between the maximum and minimum density peaks in S_B are larger than those in S_M, indicating a more homogeneous pore distribution because of the ordering effect in S_M compared to S_B. This is consistent with previous experimental studies [36] that have shown density fluctuations in BJ printed green components, revealing a significant increase in density fluctuation for bimodal powder blends. In another study, Chen et al. [9] showed the effect of fine particles placed in the interstitial spaces between coarse particles enhancing the dispersion of coarse particles leading to lower green density of BJ printed samples. Note that agglomeration of fine particles due to van der Waals force could also cause formation of new pores and voids within the powder bed.

The schematics in Fig. 10(a) illustrates several common spatial arrangements of particles leading to dense and/or loose powder package along with the corresponding snapshots of simulation of powder beds in the current study. Experimental observations of BJ printed samples from Chen et al. [9], which are consistent with our simulation results, are shown in Figs. 10(b- d). Several types of voids in mono-modal (Fig. 10 (b)) and bi-modal samples (Figs. 10(c) and (d)) are observed due to arrangement and/or agglomeration of particles which are consistent with our findings.

Fig. 10(e) provides a quantitative basis for comparing the structural differences between S_M and S_B, highlighting how particle interactions

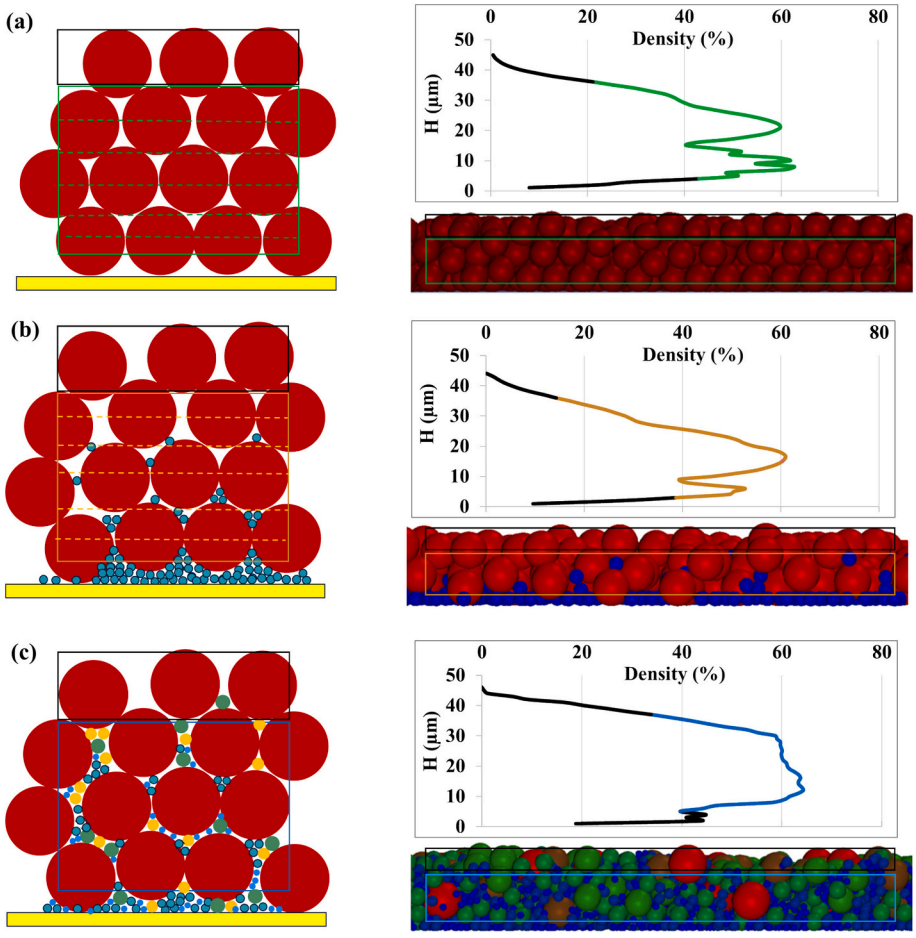

Fig. 9. Schematics showing the powder bed with density variation along the height of the first layer in a) Mono-sized sample, S_M; b) Bi-modal sample, S_B and c) powder bed with normal particles size distribution, S_P. The dashed lines for S_M and S_B samples, shown in Figs. 9 (a) and (b) represent the sub-layers within the powder layer. The black colours on the plots show regions of the powder bed in the vicinity of the substrate and free surface and they are not considered as part of the powder bed.

and distributions contribute to localized packing density and uniformity. Measuring the coordination number (*CN*) of large particles (i.e., the number of contacts between large particles) in the mono-sized and bimodal powder beds helps to determine the influence of large and small particles in formation and distribution of over- and under- populated voids that causes loose powder bed [49]. In S_M, where all particles are of similar size, the distance between large particles are relatively consistent and the average *CN* of particles inside different subdomains along the z direction is almost constant. In S_B, however, the presence of both coarse and fine particles and the associated segregation can result in a more irregular distribution of large particles. Smaller *CN* and higher distances between large particles are seen in regions close to the substrate. This is mainly due to the percolation of fine particles leading to areas with predominantly fines as well as the wedging effect and/or agglomeration of fines in over-populated states. In the regions closer to the surface of the powder bed, the under-populated regions are dominant and large particles have more contacted neighbours as shown by higher *CN*. In addition, standard deviation of coordination number along the building direction (i.e., CN_{st}) shows the degree of heterogeneity in different powder beds. While a higher *CN* indicates a denser packing arrangement with more particle interactions, larger CN_{st} implies a more heterogeneous powder bed. The schematics provided in Fig. 10(e) clearly support the quantitative results with more heterogeneous *CN* distribution along the z-axis in S_M. Note that in Fig. 10(e), the S_B powder bed snapshot does not show fine particles to demonstrate the *CN* of large particles.

Analysis of the inter-layer print-bed characteristics show that the density fluctuation in the BJ printed samples is not necessarily due to phenomena taking place between the print-layers. Density may fluctuate within the print-layers due to "ordering effect" caused by particles/voids arrangements as shown by samples printed using bi-modal and/or mono-modal powder size distributions.

It has been also shown that altering the *PSD* of powders during BJ printing process affects the packing density as well as microstructure of the printed samples. Structure of the printed sample, which is often referred to as green body, influences its sintering performance, where often the relative density and particle size are considered as critical state variables. This relationship, integral to the Process-Structure-Properties (*P-S-P*) framework, underscores how modifications at the spreading stage can be used to control the sintering process, particularly to improve densification and shape stability of the final products. Changing the parameters of printing/powder-spreading process (Process, *P*) would change the particles size and pores distributions in the green sample (Structure, *S*), hence affecting the sintering shrinkage/densification rate and final shape (Properties, *P*).

4. Conclusion

Computational methods such as the discrete element method (DEM) have been widely used to evaluate key properties like "average green density" and "average particle size" which serve as indicators of the condition of the entire powder bed in binder jet printing additive manufacturing (BJ -AM). While these properties are effective for

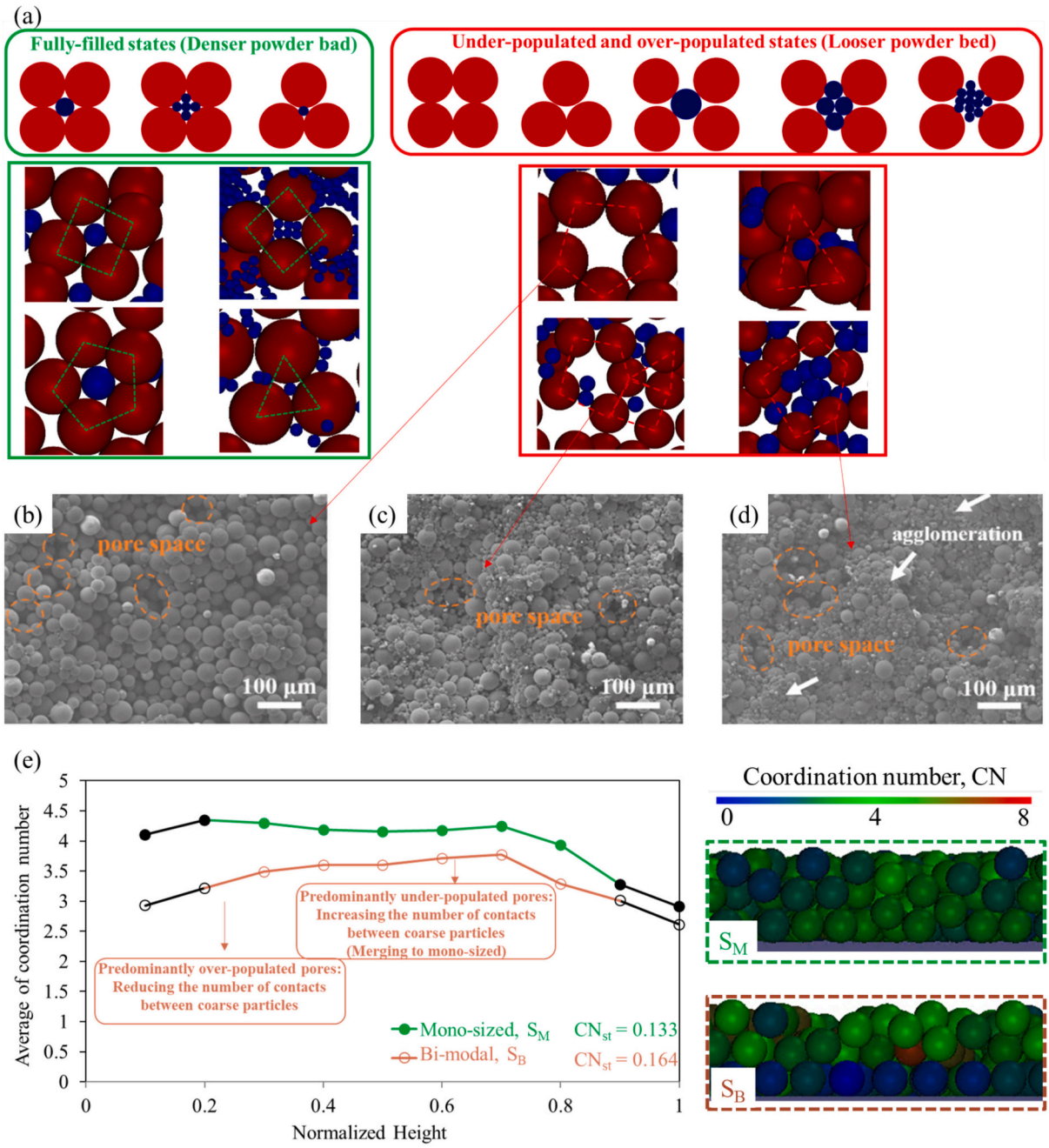

Fig. 10. a) Different spatial arrangements of particles forming dense or loose powder bed. b-d) SEM images of BJ printed green samples of unimodal and bimodal powder particles. From Ref [9], reproduced with the permission of Elsevier. e) The average of coordination number of large particles in S_M and S_B along the z direction. (For interpretation of the references to colour in this figure legend, the reader is referred to the web version of this article.)

assessing uniformly distributed print beds, they often overlook the localized phenomena within and between layers that define the overall quality of the green samples. By using DEM simulations, this study has examined both inter-layer and intra-layer microstructural properties, such as relative density and local particle sizes, in multi-layered BJ printed powder beds, focusing on how initial particle size distribution influences the development of these properties along the build direction. Accordingly, the following conclusions have been drawn:

1. Homogenous print-bed microstructures with less density fluctuations can be achieved by optimizing the particle size distributions (PSDs) with a goal of effectively filling inter-particle voids.
2. Contrary to common sense, density fluctuations are not solely a function of inter-layer interactions but also occur within print-layers. This is particularly evident in powder beds with mono-sized and/or bi-modal powders, where particles ordering can lead to uneven density distributions.
3. The study reveals different phenomena responsible for density fluctuations along the building direction.
   i. Ordering Effect: Notable within intra-layer regions in mono-sized and non-optimal bimodal powder beds, affecting particle alignment and packing efficiency.
   ii. Particles Mobility Effect: Observed in the inter-layer regions of mono-sized particles, where inter-layer pores are more likely to form.

iii. Size-ratio effect: Observed in powder beds including coarse and fine particles where particle size differences can lead to loose powder arrangements, affecting the inter-layer density.

It is also worth highlighting that by optimizing the volume fractions of the coarse and fine particles in bimodal powder, the properties of print-bed are likely to improve. In addition, controlling the translational and rotational velocities of the roller can obtain powder beds with higher relative density and uniformity. In cases where the roller has both translational and rotational motions, the rotational velocity of the roller can influence the formation of the print bed particularly when using powders with a wide PSD. This is because rotation of the roller can cause finer particles to segregate due to complex dispersion and circulation movements within the powder pile. In these regards, further studies are required to prob. the influence of process and materials parameters on the mechanisms governing the microstructural characteristics.

CRediT authorship contribution statement

Abolfazl Malti: Writing – original draft, Visualization, Validation, Software, Methodology, Investigation, Formal analysis, Conceptualization. **Christian Brandl:** Writing – review & editing, Validation, Supervision, Investigation, Formal analysis, Conceptualization. **Tesfaye Molla:** Writing – review & editing, Validation, Supervision, Resources, Project administration, Investigation, Formal analysis, Conceptualization.

Declaration of competing interest

None.

Data availability

No data was used for the research described in the article.

References

[1] P. Bourot, L. Weiss, D. Boisselier, P. Laheurte, Effect of bimodal size distribution on the behavioural properties of powders used in the LPBF process, Powder Technol. 439 (2024) 119670.
[2] W. Du, M. Singh, D. Singh, Binder jetting additive manufacturing of silicon carbide ceramics: development of bimodal powder feedstocks by modeling and experimental methods, Ceram. Int. 46 (2020) 19701–19707.
[3] H. Miyanaji, S. Zhang, L. Yang, A new physics-based model for equilibrium saturation determination in binder jetting additive manufacturing process, Int. J. Mach. Tools Manuf. 124 (2018) 1–11.
[4] M. Ziaee, N.B. Crane, Binder jetting: a review of process, materials, and methods, Addit. Manuf. 28 (2019) 781–801.
[5] A. Zocca, P. Colombo, C.M. Gomes, J. Günster, Additive manufacturing of ceramics: issues, potentialities, and opportunities, J. Am. Ceram. Soc. 98 (2015) 1983–2001.
[6] A. Mostafaei, A.M. Elliott, J.E. Barnes, F. Li, W. Tan, C.L. Cramer, P. Nandwana, M. Chmielus, Binder jet 3D printing—process parameters, materials, properties, modeling, and challenges, Prog. Mater. Sci. 119 (2021) 100707.
[7] D. Huber, L. Vogel, A. Fischer, The effects of sintering temperature and hold time on densification, mechanical properties and microstructural characteristics of binder jet 3D printed 17-4 PH stainless steel, Addit. Manuf. 46 (2021) 102114.
[8] Y. Zhu, Z. Wu, W.D. Hartley, J.M. Sietins, C.B. Williams, Z.Y. Hang, Unraveling pore evolution in post-processing of binder jetting materials: X-ray computed tomography, computer vision, and machine learning, Addit. Manuf. 34 (2020) 101183.
[9] L. Chen, W. Chen, S. Zhang, S. Zou, T. Cheng, D. Zhu, Effect of bimodal powder on densification and mechanical properties of 316L stainless steel fabricated by binder jet 3D printing, J. Mater. Res. Technol. 27 (2023) 4043–4052.
[10] S. Haeri, Y. Wang, O. Ghita, J. Sun, Discrete element simulation and experimental study of powder spreading process in additive manufacturing, Powder Technol. 306 (2017) 45–54.
[11] L. Chen, W. Chen, Z. Fu, G. Ding, Z. Chen, D. Zhu, Binder jet 3D printing of 316L stainless steel: orthogonal printing and sintering process optimization, Adv. Eng. Mater. 25 (2023) 2200641.
[12] R. Xu, W. Nan, Analysis of the metrics and mechanism of powder spreadability in powder-based additive manufacturing, Addit. Manuf. 71 (2023) 103596.
[13] A. Cabo Rios, E. Hryha, E. Olevsky, P. Harlin, Sintering anisotropy of binder jetted 316L stainless steel: part I–sintering anisotropy, Powder Metall. 65 (2022) 273–282.
[14] A. Cabo Rios, E. Hryha, E. Olevsky, P. Harlin, Sintering anisotropy of binder jetted 316L stainless steel: part II–microstructure evolution during sintering, Powder Metall. 65 (2022) 283–295.
[15] A.C. Rios, T. Mishurova, L. Cordova, M. Persson, G. Bruno, E. Olevsky, E. Hryha, Ex-situ characterization and simulation of density fluctuations evolution during sintering of binder jetted 316L, Mater. Des. 238 (2024) 112690.
[16] H. Chen, Q. Wei, Y. Zhang, F. Chen, Y. Shi, W. Yan, Powder-spreading mechanisms in powder-bed-based additive manufacturing: experiments and computational modeling, Acta Mater. 179 (2019) 158–171.
[17] D. Yao, X. Liu, J. Wang, W. Fan, M. Li, H. Fu, H. Zhang, X. Yang, Q. Zou, X. An, Numerical insights on the spreading of practical 316 L stainless steel powder in SLM additive manufacturing, Powder Technol. 390 (2021) 197–208.
[18] D. Yao, X. An, H. Fu, H. Zhang, X. Yang, Q. Zou, K. Dong, Dynamic investigation on the powder spreading during selective laser melting additive manufacturing, Addit. Manuf. 37 (2021) 101707.
[19] A. Malti, C. Brandl, T. Molla, Role of process parameters on the effective properties of the print-bed during binder jet additive manufacturing: a discrete element method-based study, Powder Technol. 120101 (2024).
[20] K. Johnson, I. Sridhar, Adhesion between a spherical indenter and an elastic solid with a compliant elastic coating, J. Phys. D. Appl. Phys. 34 (2001) 683.
[21] W. Nan, M. Ghadiri, Numerical simulation of powder flow during spreading in additive manufacturing, Powder Technol. 342 (2019) 801–807.
[22] D. Zeng, E. Zhang, Y. Ding, Y. Yi, Q. Xian, G. Yao, H. Zhu, T. Shi, Investigation of erosion behaviors of sulfur-particle-laden gas flow in an elbow via a CFD-DEM coupling method, Powder Technol. 329 (2018) 115–128.
[23] S. Cao, Y. Qiu, X.-F. Wei, H.-H. Zhang, Experimental and theoretical investigation on ultra-thin powder layering in three dimensional printing (3DP) by a novel double-smoothing mechanism, J. Mater. Process. Technol. 220 (2015) 231–242.
[24] K.L. Johnson, K. Kendall, A. Roberts, Surface energy and the contact of elastic solids, Proc. R. Soc. Lond. A 324 (1971) 301–313.
[25] M. Dosta, V. Skorych, MUSEN: An open-source framework for GPU-accelerated DEM simulations, SoftwareX 12 (2020) 100618.
[26] C. O'Sullivan, J.D. Bray, Selecting a suitable time step for discrete element simulations that use the central difference time integration scheme, Eng. Comput. 21 (2004) 278–303.
[27] W. Nan, M. Pasha, T. Bonakdar, A. Lopez, U. Zafar, S. Nadimi, M. Ghadiri, Jamming during particle spreading in additive manufacturing, Powder Technol. 338 (2018) 253–262.
[28] Z. Xiang, M. Zhang, R. Yan, Q. Yin, K. Zhang, Powder-spreading dynamics and packing quality improvement for laser powder bed fusion additive manufacturing, Powder Technol. 389 (2021) 278–291.
[29] S. Wu, Y. Yang, Y. Huang, C. Han, J. Chen, Y. Xiao, Y. Li, D. Wang, Study on powder particle behavior in powder spreading with discrete element method and its critical implications for binder jetting additive manufacturing processes, Virtual Phys. Prototyp. 18 (2023) 2158877.
[30] H. Chen, Q. Wei, S. Wen, Z. Li, Y. Shi, Flow behavior of powder particles in layering process of selective laser melting: numerical modeling and experimental verification based on discrete element method, Int. J. Mach. Tools Manuf. 123 (2017) 146–159.
[31] A. Mussatto, R. Groarke, A. O'Neill, M.A. Obeidi, Y. Delaure, D. Brabazon, Influences of powder morphology and spreading parameters on the powder bed topography uniformity in powder bed fusion metal additive manufacturing, Addit. Manuf. 38 (2021) 101807.
[32] H. Chen, Y. Chen, Y. Liu, Q. Wei, Y. Shi, W. Yan, Packing quality of powder layer during counter-rolling-type powder spreading process in additive manufacturing, Int. J. Mach. Tools Manuf. 153 (2020) 103553.
[33] M.H. Sehhat, A. Mahdianikhotbesara, Powder spreading in laser-powder bed fusion process, Granul. Matter 23 (2021) 89.
[34] R.W. Penny, P.M. Praegla, M. Ochsenius, D. Oropeza, R. Weissbach, C. Meier, W. A. Wall, A.J. Hart, Spatial mapping of powder layer density for metal additive manufacturing via transmission X-ray imaging, Addit. Manuf. 46 (2021) 102197.
[35] M. Li, G. Miao, W. Du, Z. Pei, C. Ma, Difference between powder bed density and green density for a free-flowing powder in binder jetting additive manufacturing, J. Manuf. Process. 84 (2022) 448–456.
[36] E. Wheat, M. Vlasea, J. Hinebaugh, C. Metcalfe, Sinter structure analysis of titanium structures fabricated via binder jetting additive manufacturing, Mater. Des. 156 (2018) 167–183.
[37] N.D. Parab, J.E. Barnes, C. Zhao, R.W. Cunningham, K. Fezzaa, A.D. Rollett, T. Sun, Real time observation of binder jetting printing process using high-speed X-ray imaging, Sci. Rep. 9 (2019) 2499.
[38] C. Zheng, A. Mostafaei, P.R. de Vecchis, I. Nettleship, M. Chmielus, Microstructure evolution for isothermal sintering of binder jet 3D printed alloy 625 above and below the solidus temperature, Addit. Manuf. 47 (2021) 102276.
[39] U. Ali, Y. Mahmoodkhani, S.I. Shahabad, R. Esmaeilizadeh, F. Liravi, E. Sheydaeian, K.Y. Huang, E. Marzbanrad, M. Vlasea, E. Toyserkani, On the measurement of relative powder-bed compaction density in powder-bed additive manufacturing processes, Mater. Des. 155 (2018) 495–501.
[40] A. Mostafaei, P.R. De Vecchis, I. Nettleship, M. Chmielus, Effect of powder size distribution on densification and microstructural evolution of binder-jet 3D-printed alloy 625, Mater. Des. 162 (2019) 375–383.
[41] S.B. Ojea, J. Torrents-Barrena, M.T. Pérez-Prado, R.M. Moreno, F. Sket, Binder jet green parts microstructure: advanced quantitative analysis, J. Mater. Res. Technol. 23 (2023) 3974–3986.
[42] P. Shakor, S. Chu, A. Puzatova, E. Dini, Review of binder jetting 3D printing in the construction industry, Progr. Addit. Manufact. 7 (2022) 643–669.

[43] R.M. German, S.J. Park, Handbook of Mathematical Relations in Particulate Materials Processing: Ceramics, Powder Metals, Cermets, Carbides, Hard Materials, and Minerals, John Wiley & Sons, 2008.
[44] S. Afazov, A. Roberts, L. Wright, P. Jadhav, A. Holloway, H. Basoalto, K. Milne, N. Brierley, Metal powder bed fusion process chains: an overview of modelling techniques, Progr. Addit. Manufact. (2022) 1–26.
[45] Q. Chen, E. Juste, M. Lasgorceix, F. Petit, A. Leriche, Binder jetting process with ceramic powders: influence of powder properties and printing parameters, Open Ceram. 9 (2022) 100218.
[46] R. Benenati, C. Brosilow, Void fraction distribution in beds of spheres, AICHE J. 8 (1962) 359–361.
[47] J.B. Rosenholm, Sizing and packing of particles–characterization of mono-, di-and trimodal particle assemblies, Adv. Colloid Interf. Sci. 315 (2023) 102887.
[48] K. Nygård, Local structure and density fluctuations in confined fluids, Curr. Opin. Colloid Interface Sci. 22 (2016) 30–34.
[49] E. Stevens, S. Schloder, E. Bono, D. Schmidt, M. Chmielus, Density variation in binder jetting 3D-printed and sintered Ti-6Al-4V, Addit. Manuf. 22 (2018) 746–752.